# Intrinsic Energy and Time Resolution of the Jefferson Lab Hall C Neutral Particle Spectrometer

W. Hamdi<sup>a</sup>, J. Crafts<sup>b</sup>, H. Huang<sup>c</sup>, Z. Huang<sup>d</sup>, M. Kerver<sup>e</sup>, M. Mathison<sup>f</sup>, C. Ploen<sup>e</sup>, A. Singh<sup>b</sup>, T. Song<sup>g</sup>, Y. Zhang<sup>h</sup>, D. Adhikari<sup>i</sup>, A. Ahmed<sup>ae</sup>, H. Albataineh<sup>j</sup>, K. Aniol<sup>k</sup>, J. Arrington<sup>l</sup>, A. Asaturyan<sup>m</sup>, C. Ayerbe Gayoso<sup>e</sup>, P. Bosted<sup>s</sup>, E. Brash<sup>n</sup>, S. Buelthmann<sup>e</sup>, A. Camsonne<sup>m</sup>, J. Caylor<sup>m</sup>, F. Chahili<sup>o</sup>, J.-P. Chen<sup>m</sup>, J. Colorado Caicedo<sup>v</sup>, M. Conaway<sup>f</sup>, C. Cotton<sup>ae</sup>, S. Covrig Dusa<sup>m</sup>, P. Datta<sup>p</sup>, M. Defurne<sup>q</sup>, B. Devkota<sup>aj</sup>, M. Dlamini<sup>r</sup>, D. Dutta<sup>aj</sup>, R. Ent<sup>m</sup>, E. Fuchey<sup>s</sup>, B. Gamage<sup>m</sup>, D. Gaskell<sup>m</sup>, P. Gautam<sup>ae</sup>, Y. Ghandilyan<sup>b</sup>, C. Ghosh<sup>m</sup>, T. Gogami<sup>t</sup>, D. Hamilton<sup>u</sup>, O. Hansen<sup>m</sup>, M. Hashemi Shabestari<sup>ak</sup>, N. Heinrich<sup>ah</sup>, W. Henry<sup>m</sup>, D. Higinbotham<sup>m</sup>, I. Higuera Angulo<sup>v</sup>, A. Hoghmrtsyan<sup>w</sup>, T. Horn<sup>b</sup>, G. Huber<sup>ah</sup>, C.E. Hyde<sup>e</sup>, H.-S. Jo<sup>1</sup>, M. K. Jones<sup>m</sup>, M. Junaid<sup>ah</sup>, N. Kalantarians<sup>x</sup>, S. Kay<sup>y</sup>, P. King<sup>f</sup>, E. Kinney<sup>z</sup>, S. Kundu<sup>aa</sup>, C. Lee<sup>1</sup>, W.B. Li<sup>ab</sup>, S. Li<sup>1</sup>, P.-J. Lin<sup>ac</sup>, H. Liu<sup>m</sup>, D. Mack<sup>m</sup>, S. Malace<sup>m</sup>, R. Marinaro<sup>u</sup>, M. Mazouz<sup>a</sup>, R. Michaels<sup>m</sup>, A. Mkrtchyan<sup>w</sup>, H. Mkrtchyan<sup>w</sup>, B. Moffit<sup>m</sup>, R. Montgomery<sup>u</sup>, C. Morean<sup>m,b</sup>, M. Niculescu<sup>ad</sup>, C. Muñoz Camacho<sup>c</sup>, M. Nycz<sup>ae</sup>, J. O'Kronley<sup>af</sup>, A. Panta<sup>m</sup>, R. Paremuzyan<sup>m</sup>, S. Park<sup>m</sup>, P. Pichard<sup>ag</sup>, A.C. Postuma<sup>ah</sup>, J. Poudel<sup>m</sup>, H. Presley<sup>ae</sup>, R. Reedy<sup>f</sup>, J. Reinhold<sup>ak</sup>, J. Roche<sup>f</sup>, D. Ruth<sup>ai</sup>, N. Santiesteban<sup>ai</sup>, A. Sen<sup>f</sup>, Iu. Skorodumina<sup>m</sup>, H. Szumila-Vance<sup>ak</sup>, A.S. Tadepalli<sup>m</sup>, B. Tamang<sup>aj</sup>, L. Tang<sup>m</sup>, D. Upton<sup>m</sup>, G. Villegas<sup>ak</sup>, H. Voskanyan<sup>w</sup>, E. Voutier<sup>c</sup>, B. Wojtsekhowski<sup>m</sup>, S. Wood<sup>e</sup>, E. Wrightson<sup>aj</sup>, Z. Ye<sup>d</sup>, Z. Ye<sup>h</sup>, X. Zheng<sup>ac</sup>

<sup>a</sup>Monastir University, Faculty of Sciences of Monastir, LPQS Laboratory, Monastir 5019, Tunisia <sup>b</sup>The Catholic University of America, Washington, DC 20064, USA <sup>c</sup>IJCLab, Université Paris-Saclay, Orsay 91405, France <sup>d</sup>University of Illinois Chicago, Chicago IL 60607, USA <sup>e</sup>Old Dominion University, Norfolk, VA 23529, USA <sup>f</sup>Ohio University, Athens OH 45701, USA <sup>8</sup>Kyungpook National University, Daegu 41566, Korea <sup>h</sup>Tsinghua University, Beijing 100084, China <sup>i</sup>Virginia Polytechnic Institute and State University, Blacksburg VA 24061, USA <sup>j</sup>Texas A & M University, Kingsville TX 78363, USA <sup>k</sup>California State University, Los Angeles CA 90032, USA <sup>1</sup>Lawrence Berkeley Laboratory, Berkeley CA 94720, USA <sup>m</sup>Thomas Jefferson National Accelerator Facility, Newport News VA 23606, USA <sup>n</sup>Christopher Newport University, Newport News VA 23606, USA OSyracuse University, Syracuse NY 13244, USA <sup>p</sup>University of Connecticut, Storrs CT 06269, USA <sup>q</sup>CEA Saclay, Gif-sur-Yvette 91191, France <sup>r</sup>University of Eswatini, Kwaluseni M201, Eswatini <sup>s</sup>The College of William and Mary, Williamsburg VA 23187, USA <sup>t</sup>Kyoto University, Kyoto 606-8501, Japan <sup>u</sup>University of Glasgow, Glasgow G12 8QQ, United Kingdom VCINVESTAV, Mexico City 07360, Mexico <sup>w</sup>A.I. Alikhanyan National Science Laboratory (Yerevan Physics Institute), Yerevan 0036, Armenia <sup>x</sup>Virginia Union University, Richmond VA 23220, USA <sup>y</sup>University of York, York YO10 5DD, United Kingdom <sup>z</sup>University of Colorado, Boulder CO 80309, USA <sup>aa</sup>Indiana University, Bloomington IN 47405, USA <sup>ab</sup>Mississippi State University, Mississippi State, Mississippi 39762, USA ac National Central University, Taoyuan City 32001, Taiwan <sup>ad</sup> James Madison University, Harrisonburg VA 22807, USA ae University of Virginia, Charlottesville VA 22904, USA af University of Tennessee, Knoxville TN 37996, USA ag Universit de Nantes, Nantes 44000, France <sup>ah</sup>University of Regina, Regina SK S4S 0A2, Canada <sup>ai</sup> University of New Hampshire, Durham NH 03824, USA <sup>aj</sup>Mississippi State University, Mississippi State MS 39762, USA <sup>ak</sup>Florida International University, Miami FL 33199, USA

# Abstract

The Neutral Particle Spectrometer (NPS) is an advanced calorimeter designed to measure neutral electromagnetic particles with high precision in energy, time, and position, under conditions of high luminosity and significant background. Integrated into the experimental setup of Hall C at Thomas Jefferson National Accelerator Facility, the NPS plays a critical role in studies of nucleon structure through exclusive and semi-inclusive reaction channels. This paper presents an assessment of the detector's performance characteristics, specifically its energy and timing resolution, derived from elastic electron-proton scattering data. We report an energy resolution between 1.2% and 1.3% in the 4.5–7.3 GeV range, and an intrinsic timing resolution better than 200 ps for energies above 500 MeV. These results serve as a reference for current and future precision measurements in hadronic physics.

*Keywords:* Electromagnetic calorimetry, Neutral Particle Spectrometer, Time resolution, Energy resolution, Elastic scattering, Detector performance, Hall C, Thomas Jefferson National Accelerator Facility

#### 1. Introduction

The study of exclusive reactions at high energies provides a powerful tool to probe the internal structure of hadrons in terms of quark and gluon degrees of freedom [1]. Processes such as deeply virtual Compton scattering (DVCS) [2] and deep exclusive meson production (DEMP) [3, 4] grant access to Generalized Parton Distributions (GPDs) [5, 6, 7], which encode correlations between parton longitudinal momentum and transverse spatial position offering a three-dimensional imaging of the nucleon [8]. Achieving high precision in these measurements requires the detection of photons and neutral mesons with excellent energy and timing resolution, particularly in high luminosity environments where backgrounds can obscure rare processes.

The Neutral Particle Spectrometer (NPS) was developed as a state of the art detection system to fulfill this need within the Hall C experimental program at Thomas Jefferson National Accelerator Facility. Comprising a dense array of PbWO4 crystals [9] coupled to high-resolution readout electronics, the NPS enables accurate measurements of electromagnetic final states with fine spatial granularity and sub-nanosecond timing precision [10]. Its modular design supports flexible angular positioning and distance adjustments to accommodate a broad range of kinematic settings. This work presents the intrinsic performance of the lead tungstate crystals obtained using elastic calibration data. We focus on the extraction of energy and time resolution across a wide energy range, leveraging waveform analysis techniques and clustering algorithms to reconstruct signals with high fidelity. The results obtained demonstrate the capability of the NPS to meet the stringent requirements of the 12 GeV physics program at Thomas Jefferson National Accelerator Facility, and provide a benchmark for its deployment in experiments aimed at mapping the nucleon's internal structure.

The paper is organized as follows: the following section de- 65 scribes the experimental setup, including the NPS, the High Momentum Spectrometer (HMS), the trigger and readout system, and the elastic calibration method. Section 3 details the data analysis procedures, covering waveform processing, time alignment, clustering, elastic event selection in HMS, and energy calibration. Finally, section 4 presents the main results, 70 focusing on energy and time resolution measurements.

# 2. Experimental Setup

# 2.1. Neutral Particle Spectrometer (NPS)

The Neutral Particle Spectrometer is a high-resolution electromagnetic calorimeter designed for precision measurements of gamma-rays. It consists of 1080 high-quality PbWO<sub>4</sub> crystals  $(2.05\times2.05\times20~\text{cm}^3)$  arranged in a  $36\times30$  tower matrix <sup>80</sup> (Figure 1). The calorimeter is mounted on a movable platform using the Super High Momentum Spectrometer (SHMS) carriage, allowing variable positioning at different distances from the target and angular coverage between  $6^\circ$  and  $25^\circ$ . PbWO<sub>4</sub> crystals were selected for their excellent calorimetric propersies, including a small Molière radius ( $R_M = 2.19~\text{cm}$ ) and short radiation length ( $L_R = 0.89~\text{cm}$ ), resulting in high granularity. This makes them ideal for reconstructing electromagnetic showers in the energy range of 0.1 to 10~GeV [11]. The crystals are mechanically supported by a precision carbon matrix. Each <sup>90</sup>



Figure 1: Front view of the Neutral Particle Spectrometer (NPS). The NPS comprises a  $36 \times 30$  matrix of PbWO<sub>4</sub> crystals and is placed inside a black box to prevent light leakage.

crystal is optically coupled to a Hamamatsu R4125 photomultiplier tube (PMT). PMTs are equipped with a custom high voltage active bases that include built in pre-amplifiers [13]. Thermal stability is also maintained to prevent temperature-induced light-yield fluctuations. The readout system features deadtimeless digitizing electronics, ensuring precise waveform acquisition for all channels in high-luminosity environments.

## 2.2. High Momentum Spectrometer (HMS)

The HMS plays a central role in the reconstruction of scattering events in Hall C experiments at Thomas Jefferson National Accelerator Facility [14]. As a magnetic spectrometer designed to detect and identify charged particles, primarily electrons, the HMS provides precise measurements of momentum, angle, and trajectory, which are essential for exclusive reaction studies [15]. In all the approved experiments involving the Neutral Particle Spectrometer (NPS), the HMS is used to detect the scattered electron in coincidence with photons or neutral mesons observed in the NPS (Figure 2), enabling full kinematic reconstruction of the event. The spectrometer includes a set of quadrupole and dipole magnets, coupled with drift chambers for tracking, scintillator planes for timing, Cerenkov and calorimeter detectors for particle identification as shown in Figure 3. The HMS can be rotated to angles as low as 10.5° and as high as 90°, covering momentum ranges from 0.5 GeV/c to over 7 GeV/c. This flexibility makes it invaluable for mapping cross-sections across a wide kinematic domain.

In the context of triggering, the HMS scintillator planes provide fast timing signals used in coincidence with the NPS to form the Level-1 hardware trigger. The timing precision of the HMS is critical for identifying valid coincidence events and for rejecting accidental background, especially in high luminosity experiments [17, 18]. Its well-understood optics and stable performance over decades of operation provide a reliable anchor

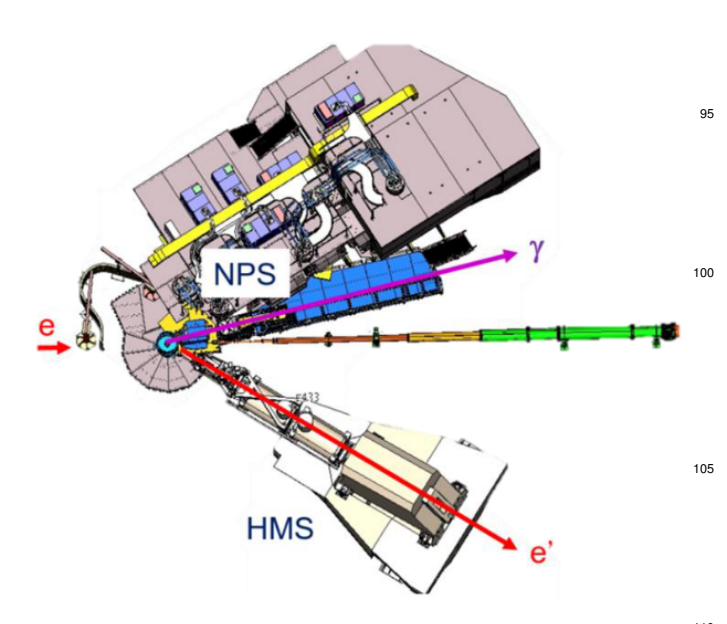


Figure 2: NPS calorimeter and HMS spectrometer in Hall C. The NPS is 110 mounted on the SHMS carriage. In the DVCS experiment, an electron beam coming from the left interacts with the target, producing a photon that is measured by the NPS. The coincident scattered electron is tracked and momentum-analyzed by the HMS.

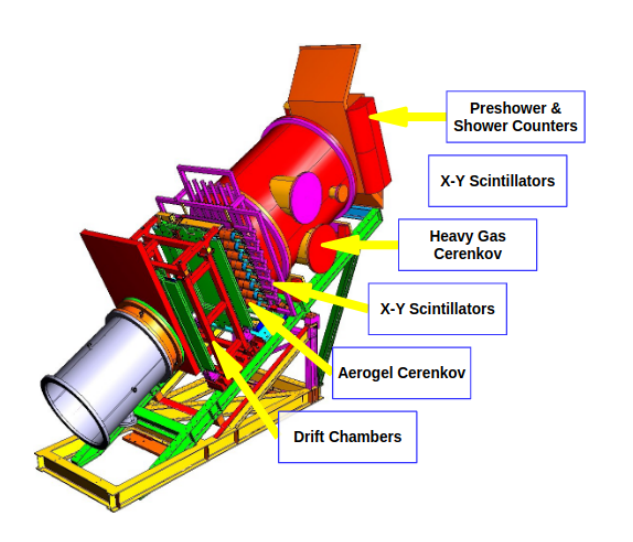


Figure 3: HMS focal-plane detectors. Particles enter from the lower left and tra-<sup>125</sup> verse toward the upper right. The gas Cherenkov and electromagnetic calorimeter provide particle identification (PID), the two scintillator hodoscope planes supply the trigger (and time of flight reference), and the drift chambers deliver precise tracking of the trajectories. [16].

for multi-detector setups, and its resolution in momentum and timing ensures accurate vertex and energy reconstruction.

#### 2.3. Triggering System and Signal Processing in NPS

A comprehensive description of the NPS Hardware and triggering system will be presented in a future publication. All 1080 PbWO<sub>4</sub> channels are digitized by the deadtime-less fADC250 modules with 12-bit resolution at 250 MHz. FPGA processors identify pulses above a programmable threshold and find clusters within 3 × 3 arrays around each seed crystal. In response to either an HMS trigger or combined NPS∩HMS coincidence trigger, waveforms are written to the external data file.

# 2.4. Elastic Calibration Settings

Elastic electron-proton scattering events serve as a fundamental benchmark for calibrating the energy response of NPS. In this clean and well-understood two-body process, a high-energy electron elastically scatters off a stationary proton in a liquid hydrogen target, transferring energy and momentum without inducing particle production or internal excitation. The resulting final-state kinematics are precisely determined by conservation of energy and momentum, making elastic scattering ideal for establishing calibration baselines.

In the experimental setup for NPS calibration, the recoil proton is detected by the HMS, which provides high-resolution tracking and momentum reconstruction. Simultaneously, the scattered electron is intercepted by the NPS, where it initiates an electromagnetic shower in the PbWO $_4$  crystal matrix. The total energy deposited by this shower is collected across the impacted crystals, forming a compact energy cluster. By correlating the measured proton momentum from the HMS with the expected electron energy using elastic kinematics, one can accurately predict the electron energy that the NPS should register for each event j:

$$E_j = E_b + m - E_j^p, \tag{1}$$

where  $E_b$  is the electron beam energy, m is the proton mass, and  $E_j^p$  is the energy of the recoiling proton in event j determined from HMS tracking. The comparison between this expected energy and the NPS response serves to determine the calibration coefficients of the NPS blocks, as will be explained in section 3.5. Table 1 lists the kinematics of the elastic settings performed during the NPS suite of DVCS and SIDIS experiments that ran September 2023 to May 2024. The NPS distance to the target, which varied from 8.0 to 9.5 m depending on the setting, was adjusted to match the elastic scattered protons in the HMS acceptance. During each setting, the NPS crystal temperature was stable to within 0.1°C, which ensured a light-yield variation of no more than 0.25 % [22].

# 3. Data Analysis

## 3.1. Waveform Analysis

Precise signal reconstruction is an important factor during experiments such as DVCS, where accurate timing and energy measurements of neutral particles are essential to resolve

Table 1: Kinematic settings for the elastic measurements. Values represent either the mean or a range (min-max) depending on the observed variation across the corresponding data set.

Number of settings	Beam energy	HMS Momentum	HMS angle	Scattered electron energy	NPS angle
	(GeV)	(GeV/c)	(degree)	(GeV)	(degree)
2	6.40	2.62	35.96	4.52–4.53	18.31–21.16
2	8.48	3.58-4.07	27.61–30.76	5.24-5.70	19.84–22.96
5	10.54	4.05-4.31	29.67-29.86	7.27–7.35	12.11–18.16

pile-up, achieve optimal resolution and thus distinguish exclusive reactions from semi-inclusive ones. In the case of the NPS calorimeter, where the 1080 channels are coupled to high frequency sampling fADCs, the analysis of digitized waveforms is necessary to extract the arrival time and amplitude of pulses produced by electromagnetic showers. Waveform analysis enables event-by-event reconstruction of pulse characteristics, even in the presence of noise or overlapping signals. Traditional peak finding or threshold techniques may suffer in high rate environments or fail to resolve closely spaced pulses. For this reason, we adopt the matched filter technique, used for instance to detect gravitational waves [23, 24], which is a digital signal processing approach that maximizes the signal to noise ratio by correlating the recorded waveform with a known reference shape. The reference pulse shapes are obtained from a sample of clean, isolated pulses selected from elastic calibration runs. These reference shapes, which obey a few precise criteria (highest amplitude pulse, no pile ups and within +/-20 ns from the coincidence time window) are normalized to 1mV amplitude and stored for each crystal channel. Figure 4 shows an example of a reference shape for a given NPS channel. Spline interpolation [25] is performed on the 110 samples of each reference waveform to generate a continuous function that will subsequently be used to fit the waveforms. For a given waveform, a matched filter response is computed by sliding the time-reversed reference shape across the recorded signal and calculating the dot product (convolution) at each time bin. This operation highlights the time positions where the incoming signal best matches the expected shape. The matched filter for each crystal is obtained from eleven peak values of the reference waveform, as illustrated in Figure 4.

Figure 5 shows an example of a signal waveform and its matched filter transform. The time corresponding to a peak in the matched filter output provides the approximate arrival time of the pulse, while the height of the response is proportional to the pulse amplitude. To increase precision, we perform a fit of the entire original waveform using a superposition of multiple reference shapes to refine the amplitude and arrival time of each pulse. The free parameters of this fit are the baseline level, and the amplitudes and arrival times of all pulses initially identified by the matched filter. An example of a waveform fit is shown in Figure 5.

## 3.2. Time correction

To achieve good coincidence time resolution, the raw pulse time  $t_{\text{raw}}^{j,i}$ , determined by the waveform fit procedure for a given event j and NPS channel i, must be corrected. This  $t_{\text{raw}}^{j,i}$  repre-

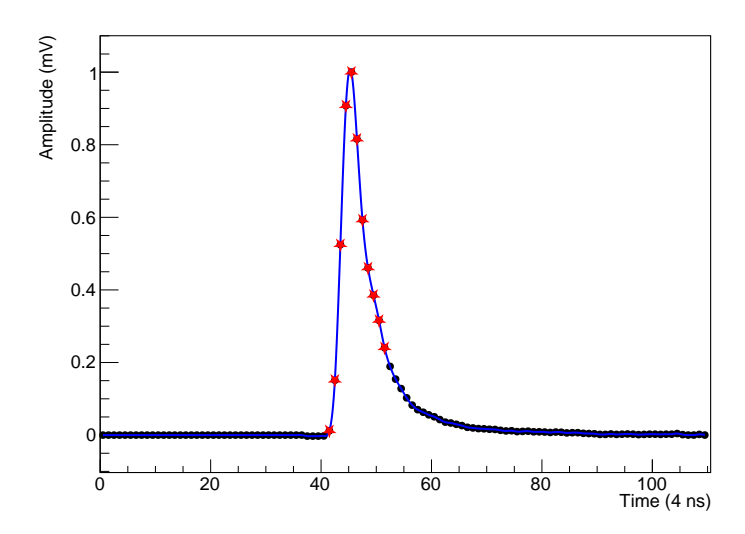


Figure 4: Reference shape pulse (black markers) and its Spline interpolation (blue curve). This reference waveform is obtained from elastic  $H(e, e'_{NPS}p_{HMS})$  data. Eleven highlighted samples (red stars) illustrate the matched filter obtained from this reference pulse.

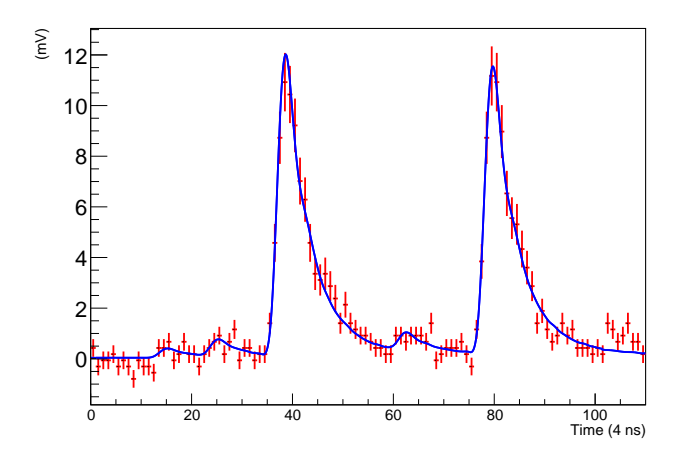
sents, up to a constant, the time difference between the arrival of the particle that triggered the HMS and the arrival of the particle that induced a pulse in an NPS channel. These corrections account for various factors, including a time offset  $t_{\rm offset}^i$  unique to each NPS channel i and an HMS correction  $t_{\rm HMS}^j$  dependent on the particle time of flight and signal processing in the HMS:

$$t_{\text{corr}}^{\mathbf{j},\mathbf{i}} = t_{\text{raw}}^{\mathbf{j},\mathbf{i}} + t_{\text{offset}}^{\mathbf{i}} + t_{\text{HMS}}^{\mathbf{j}}.$$
 (2)

The different offsets  $t_{\rm offset}^{\rm i}$  are determined from the coincidence peak position (obtained with a Gaussian fit) in the  $t_{\rm raw}^{\rm i} + t_{\rm HMS}$  distributions and are adjusted to yield a  $t_{\rm corr}^{\rm i}$  distribution centered at zero. Figure 6 shows an example of the  $t_{\rm corr}$  distribution for all NPS channels, specifically for pulses with amplitude higher than 50 mV (corresponding approximately to an energy deposit higher than 500 MeV). All the accidental peaks were fitted with common height and spacing. The obtained coincidence time resolution is 0.35 ns, which clearly reveals the 2 ns bunch structure of the electron beam.

## 3.3. Clustering

The goal of the offline clustering used in the elastics study is to group fired NPS blocks into adjacent sets where the electromagnetic shower, induced by a particle, has spread. The algorithm begins by considering only NPS blocks with pulses in



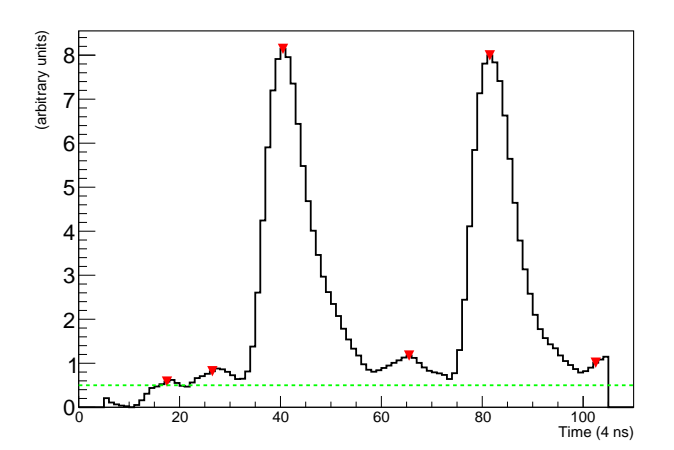


Figure 5: Example of a waveform signal (top) and its matched filter trans- $_{200}$  form (bottom). In the matched filter transform, red markers indicate identified peaks above a given threshold represented by the dotted green line. The blue curve represents the fit of the waveform using multiple reference shapes, guided by the peak identification from the matched filter (pulses at the edge of the waveform window are not fitted). This waveform example is from production  $H(e, e'_{\rm HMS}\gamma_{\rm NPS})X$  data.

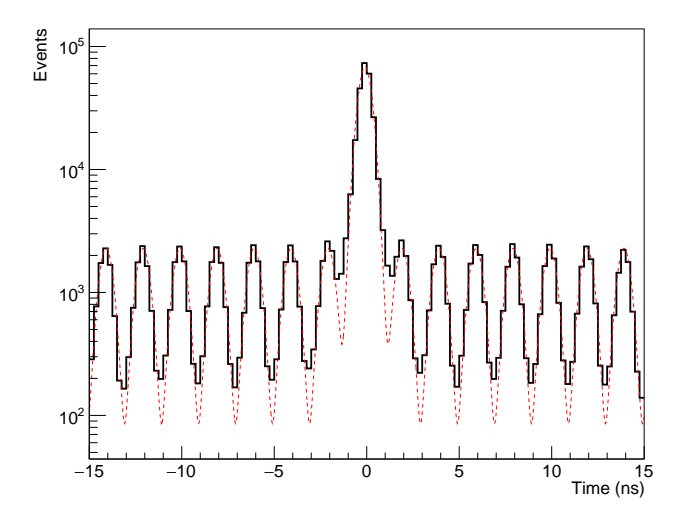


Figure 6: Corrected time distribution for pulses with amplitude higher than 50 mV. The dotted red curve represents a fit to this distribution using multiple Gaussians with a common sigma and separated by 2 ns. This fit yields a time resolution of 0.35 ns.

coincidence with the HMS and that satisfy a mild timing condition:

$$|t_{\rm corr}^i| < 5 \times \sigma_i \quad , \tag{3}$$

where  $\sigma_i$  represents the coincidence time resolution of channel i. Subsequently, it searches for cluster seed blocks, characterized by their local maximum amplitude. The number of local maxima then represents the number of clusters found in a given event. Since the inter-block distance (2.15 cm) is roughly equal to the Molière Radius of PbWO<sub>4</sub> ( $R_M = 2.19$  cm), blocks belonging to a given cluster are considered to be at most within a 5×5 matrix of blocks centered on a seed block. A 1 mV threshold is applied to the pulse amplitude for block inclusion at this stage within this  $5 \times 5$  matrix. Once the energy calibration coefficients are known, this threshold will correspond to approximately 10 MeV. The total energy  $E = \sum_i E_i$  of the cluster is calculated as the sum of calibrated energy deposits  $E_i = C_i A_i$  in each block i of the cluster, where  $C_i$  is the calibration coefficient and  $A_i$  is the pulse amplitude. Finally, only clusters with a total energy exceeding 0.5 GeV are considered valid, based on the expected energy of the scattered electrons detailed in Table 1, to suppress low-energy background.

The transverse impact position  $\vec{x}$  of the incoming particle on NPS is estimated using the center of gravity method [26] which employs a logarithmic weighting scheme:

$$\vec{x} = \frac{\sum_{i} w_{i} \vec{x}_{i}}{\sum_{i} w_{i}}, \quad w_{i} = \max \left\{ 0, W_{0} + \ln \left( \frac{E_{i}}{E} \right) \right\}$$
 (4)

where  $\vec{x_i}$  represents the block center coordinates and  $W_0$  is a tunable constant that depends on the shower total energy E. It is further parameterized as [27]:

$$W_0 = \ln\left(\frac{100 \, E(\text{GeV})}{2.02 \, e^{-\frac{d}{R_M}} + \left[4.98 \, e^{-\frac{d}{R_M}} + 0.30\right] E(\text{GeV})}\right) \tag{5}$$

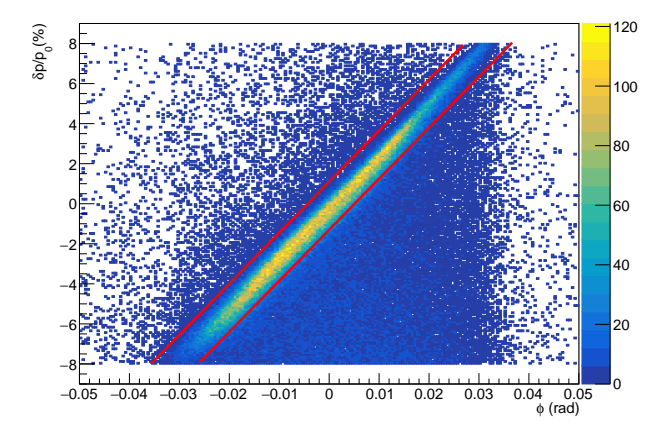


Figure 7: Two-dimensional distribution of relative momentum deviation  $\delta p/p_0$  from the HMS central momentum value versus azimuthal angle  $\phi$  measured in the HMS for elastic proton candidates. The red band corresponds to elastic scattering events that follow the optical correlation between momentum and angle.

with d being the crystal size. The spatial resolution of the NPS is expected to be below 2.5 mm for photon energies higher than 0.5 GeV [27, 28]. The depth a of the shower centroid is estimated from its energy with the following formula, which was derived from a GEANT4 simulation study:

$$a(\text{cm}) = \frac{5.079 \cdot 10^{-3}}{1 - 7.62 \cdot 10^{-4} - e^{-1.07 \cdot 10^{-3} \times E(\text{GeV})}} + 9.316 \quad (6)$$

Once the cluster energy and centroid coordinates are known, the 4-vector of the particle detected in the NPS (electron or photon) can be determined using the target vertex coordinates.

## 3.4. Elastic event selection in the HMS

Elastic events are selected using a strict HMS 2D cut to isolate elastic interactions as shown in Figure 7. This cut, and additional acceptance cuts are defined as follows:

$$|\theta| < 0.08 \text{ rad}, \quad |\phi| < 0.04 \text{ rad}, \quad |\delta p/p_0| < 8\%,$$

$$(250\%) \cdot \phi(\text{mr}) - 2\% < \delta p/p_0 < (250\%) \cdot \phi(\text{mr}) + 1\%,$$

$$|z| < 4 \text{ cm},$$
(7)

where  $\theta$  and  $\phi$  are the scattering angles in the vertical and horizontal planes respectively,  $\delta p/p_0$  is the relative momentum deviation from the HMS central momentum value, and z is the reconstructed vertex position in the target along the beamline. The cuts on  $\theta$ ,  $\phi$  and  $\delta p/p_0$  variables serve to remove events at the edge of the HMS acceptance, while the cut on |z| is applied to remove events from the target walls. These cuts retain only high-quality elastic scattering candidates.

# 3.5. Energy calibration

## 3.5.1. First pass

At this stage, elastic events H(e,e'<sub>NPS</sub> p<sub>HMS</sub>) are selected as described in the previous section, and the corresponding scattered electron clusters in the NPS are identified. In the first

energy calibration pass, only the pulse amplitudes  $A_{ij}$  (in mV) for NPS channel i and event j that belongs to an NPS cluster are known. The goal is to transform these amplitudes into energy deposits  $E_{ij}$  using the calibration coefficients  $C_i$ . For this purpose, a minimization procedure is employed to determine the calibration coefficients for each block. We define a  $\chi^2$  function over N elastic events:

$$\chi^{2} = \sum_{i=1}^{N} \left( E_{j} - \sum_{i} C_{i} \cdot A_{ij} \right)^{2}, \tag{8}$$

where  $E_j$  is the expected electron energy as given in Equation 1. Minimizing  $\chi^2$  with respect to each  $C_k$  leads to a system of 1080 linear equations (one per block):

$$\sum_{i} \left[ \sum_{j=1}^{N} A_{ij} A_{kj} \right] C_{i} = \sum_{j=1}^{N} E_{j} A_{kj}.$$
 (9)

Solving this matrix equation provides the optimal gain factors  $C_i$ .

#### 3.5.2. Subsequent passes

The goal of the subsequent energy calibration passes is to refine the selection of elastic events used to calibrate the calorimeter. Once the deposited energies in NPS blocks are known with relatively good precision, one can compute the scattered electron's 3-momentum as described in Section 3.3. This computed momentum can then be compared to the expected one, which is calculated from the known electron beam momentum and the scattered proton momentum measured by the HMS. For instance, an additional cut comparing the reconstructed cluster position (x, y) to the expected electron impact position  $(x_{\text{pred}}, y_{\text{pred}})$  can be applied to remove events where a significant mismatch is observed:

$$|x - x_{\text{pred}} - \langle x \rangle| < 4 \cdot \sigma_x, \quad |y - y_{\text{pred}} - \langle y \rangle| < 4 \cdot \sigma_y, \quad (10)$$

where  $\langle x \rangle$ ,  $\langle y \rangle$  are alignment offsets corresponding to the mean values of  $x - x_{pred}$  and  $y - y_{pred}$  distributions, and  $\sigma_x, \sigma_y$  are the widths of the residual distributions. Geometrical cuts are also applied to exclude seed blocks located at the calorimeter's edge where the electromagnetic shower cannot fully develop, or to exclude non-functional channels. Finally, an energy cut is applied which serves to validate the consistency of the measured energy with the expected electron energy derived from the HMS proton measurement. Since the incident or scattered electron may undergo radiative energy losses before reaching the calorimeter, its energy can be lower than the expected one calculated using Equation 1. Incorporating these events into the minimization procedure may bias the calibration coefficients. To mitigate this effect, we impose a lower-bound energy cut, typically excluding events where the measured energy in the NPS is significantly lower (at > 2-standard-deviation level) than the expected one. It should be noted that a partial energy loss of the shower can occur due to the presence of hardware/software thresholds in the clustering algorithm. Since the calibration coefficients correct for this effect only at the average

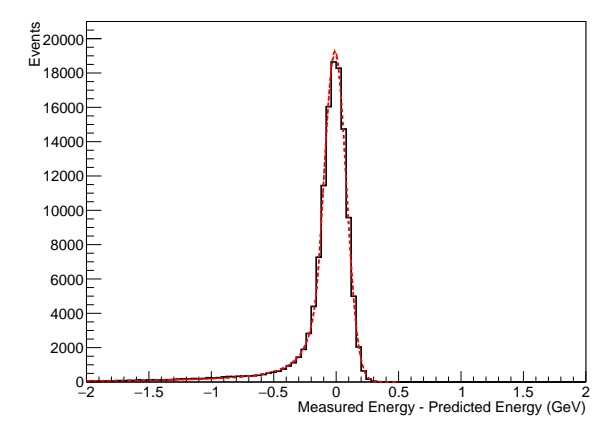


Figure 8: Histogram of the difference between the measured electron energy in the NPS and its expected energy calculated using Equation 1. The dotted red curve shows the fit of this distribution with a Crystal Ball function. The average scattered electron energy in this setting is  $\langle E \rangle = 7.3$  GeV.

scattered electron energy  $\langle E \rangle$ , an empirical correction is applied by multiplying the measured cluster energy E for each event by  $1/(1+\alpha(E-\langle E \rangle))$ , where  $\alpha=0.05$  for most elastic settings. The complete calibration cycle comprising  $\chi^2$  minimization, cuts, corrections, and re-evaluations is typically iterated five times to ensure convergence to a stable and optimal energy resolution.  $^{275}$ 

## 4. Results

#### 4.1. Energy Resolution

To assess the energy resolution performance of the NPS, the elastic calibration procedure is applied to the data from nine<sub>280</sub> elastic setting collected during the DVCS experiment in Hall C. Figure 8 shows for a given setting the difference between the measured electron energy in the NPS and its expected energy (Equation 1) after applying all the cuts and corrections detailed in the preceding sections. The distribution is fitted using a Crys-<sub>285</sub> tal Ball function [29] to determine the energy resolution and to account for the radiative tail on the low-energy side. In this example, the distribution width is equal to  $\sigma_E(E) = 90 \text{ MeV}$  leading to an energy resolution of  $\sigma_E(E)/E = 1.2\%$ 

Figure 9 summarizes the obtained energy resolution as a<sup>290</sup> function of energy for all elastic settings. The energy resolution is between 1.2% and 1.3% for nearly all settings, with an average value of 1.25%. The small discrepancy between some settings acquired at the same energy may be attributed to radiation damage to the NPS blocks during the DVCS experiment. Gen-<sup>295</sup> erally, the settings acquired at the beginning of the experiment yielded the best energy resolution. The results exhibit superior performance relative to the PrimEx PbWO<sub>4</sub> calorimeter [30] which has a similar design to the NPS with 1152 PbWO<sub>4</sub> crystals. The results also reproduce, to within 0.1%, the energy resolution reported during the 2021 test of the CCAL prototype calorimeter [11].

Overall, this performance validation across multiple energy settings confirms the NPS calorimeter's capability to deliver

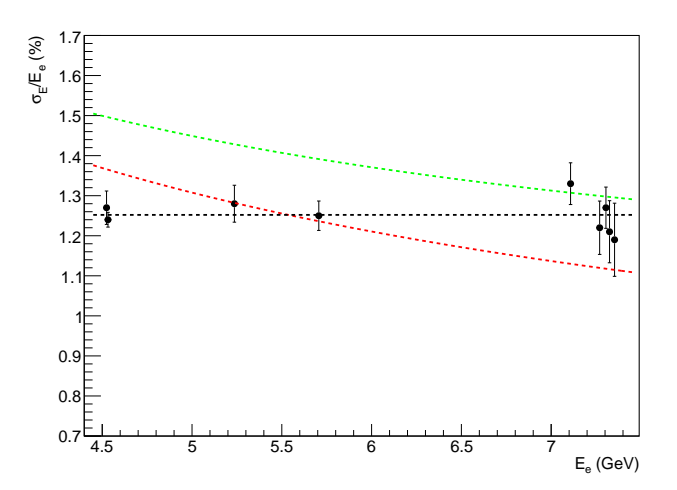


Figure 9: Energy resolution as a function of the scattered electron energy. Each error bars indicate the standard deviation from the average value (black point) across different regions of the calorimeter. The dotted green (red) line indicates the energy resolution achieved with the PrimEx PbWO4 calorimeter [30] (the CCAL prototype calorimeter [11]). The dotted black line represents a constant fit of all resolution values obtained during the experiment, yielding an average of 1.25%.

sub-1.5% energy resolution over a broad dynamic range, with temporal degradation from irradiation still within manageable bounds.

## 4.2. Time Resolution

A key performance metric of the NPS calorimeter is its intrinsic time resolution, which directly impacts the suppression of accidental coincidences in high-rate environments and the precise timing of neutral particle detection. To evaluate this, a method based on the difference in timing between calorimeter blocks belonging to the same cluster is employed, leveraging elastic calibration data. The goal is to extract the intrinsic time resolution of individual PbWO<sub>4</sub> blocks. This is achieved by selecting a large dataset of elastic events and dividing the data into multiple narrow energy intervals, each with comparable statistics. For each energy bin, all possible pairs of blocks within the same cluster and energy range are identified. The time difference  $\Delta t = t_1 - t_2$  is calculated between signals in each block pair. Figure 10 shows an example of  $\Delta t$  distribution when both pulses have an energy between 650 and 800 MeV. The  $\Delta t$  distributions are then fitted using a Gaussian function for the coincidence peak plus a constant for accidentals which are very rare in these elastic settings. The extracted width  $\sigma_{\Delta t}$  of each coincidence peak is related to the intrinsic timing resolution of individual blocks through  $\sigma_t(E) = \sigma_{\Delta t}/\sqrt{2}$ . This division accounts for the assumption that both blocks contribute equally and independently to the timing resolution.

The time resolution is studied across a wide energy spectrum, from low-energy deposits of approximately 10 MeV up to a few GeV. As shown in Figure 11, the resolution improves with increasing energy and is reproducible between different elastic settings. At low energies,  $\sigma_t(E)$  is greater than 1 ns, but drops

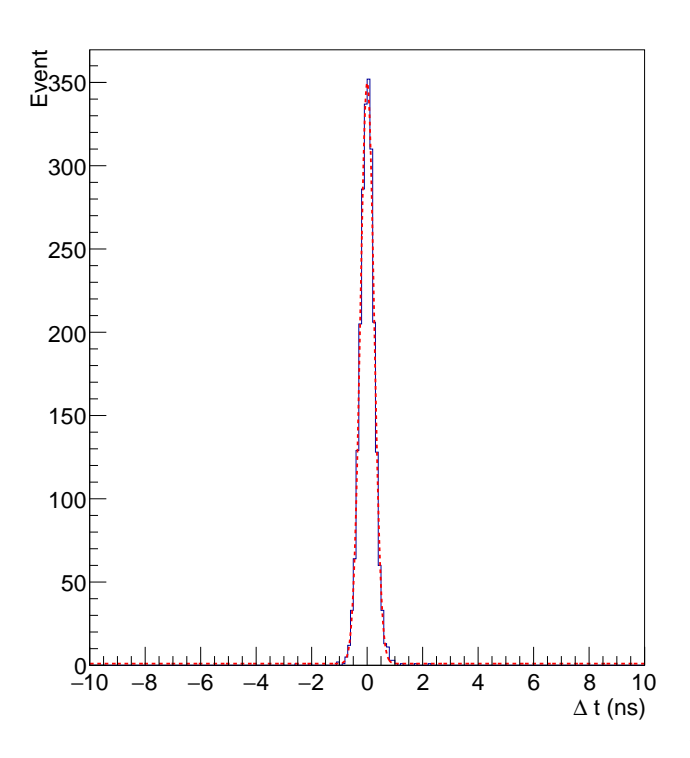


Figure 10: Time difference distribution for pulses having an energy between 650 and 800 MeV. The dotted red curve shows a fit by a Gaussian and a constant to this distribution.

below that value for energies above 70 MeV. Meanwhile, at energies greater than 500 MeV (which typically corresponds to 325 the energy of a cluster seed block), it drops below 200 ps. The energy dependence of the time resolution follows a power law between 50 MeV and 700 MeV, of the form:

$$\sigma_t(E) = (0.112 \text{ ns})[E/(1 \text{ GeV})]^{-0.845}.$$
 (11)

This result demonstrates the excellent timing capabilities of the NPS. Notably, these resolutions represent the intrinsic detector performance prior to applying global event-level corrections. The high precision achieved here enhances the separation of 335 true photon candidates from accidentals in exclusive final-state reactions and contributes to the reduction of accidental pulses in the clustering procedure, which also helps maintain good energy resolution. The method described forms the basis for 400 timing performance characterization under both low- and high-energy running conditions.

#### 5. Conclusion

The performance validation of the Neutral Particle Spectrometer (NPS) demonstrates its capability to achieve exceptional<sub>350</sub> energy and time resolution across a wide range of experimental settings. Energy resolution measurements using elastic calibration show values as low as 1.2% at 7.3 GeV. Time resolution analyses based on cluster block-pair differences confirmed ex-<sub>355</sub> cellent intrinsic performance, with resolutions dropping below

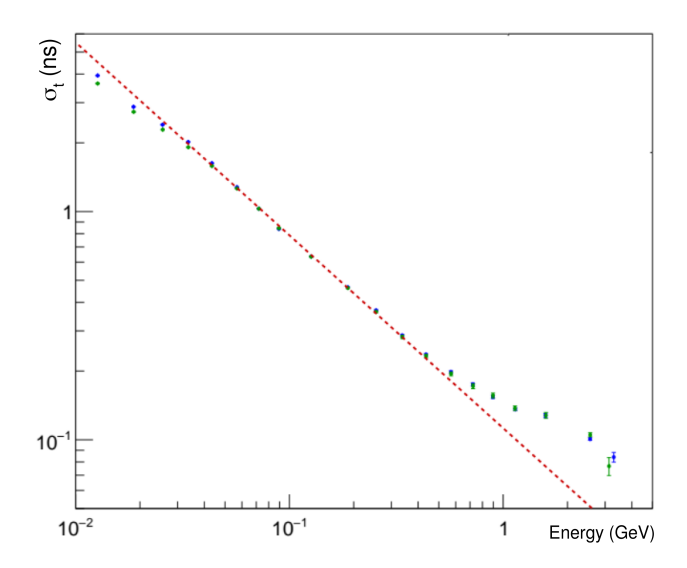


Figure 11: Intrinsic time resolution  $\sigma_t(E)$  as a function of energy. The different marker colors correspond to two different elastic settings. The dotted red curve represents the parametrization from equation 11.

200 ps at high energies. Overall, the NPS exhibits high stability and accuracy, ensuring its utility for high-precision experiments at Thomas Jefferson National Accelerator Facility.

#### Acknowledgments

We acknowledge the efforts of the staff of the Accelerator and the Physics Divisions at Jefferson Lab in making this experiment possible. This work is supported in part by the U.S. Department of Energy, the National Science Foundation (NSF), Office of Science, Office of Nuclear Physics under contract DE-FG02-96ER40960. The work of AANL group are supported by the High Education and Science Committee of RA, in the frames of the research project 21AG-1C028.

- K. Goeke, M.V. Polyakov, and M. Vanderhaeghen, Hard exclusive reactions and the structure of hadrons, Progress in Particle and Nuclear Physics 47, 401–515 (2001).
- [2] Xiangdong Ji, Deeply virtual Compton scattering, Physical Review D 55, 7114 (1997).
- [3] M. Vanderhaeghen, P.A.M. Guichon, and M. Guidal, Deeply virtual electroproduction of photons and mesons on the nucleon: Leading order amplitudes and power corrections, Physical Review D 60, 094017 (1999).
- [4] S.V. Goloskokov and P. Kroll, Vector-meson electroproduction at small Bjorken-x and generalized parton distributions, The European Physical Journal C 42, 281–301 (2005).
- [5] Markus Diehl, Generalized parton distributions, Physics Reports 388, 41–277 (2003).
- [6] Andrei V. Belitsky and A.V. Radyushkin, Unraveling hadron structure with generalized parton distributions, Physics Reports 418, 1–387 (2005).
- [7] D. Muller et al., Wave functions, evolution equations and evolution kernels from light-ray operators of QCD, Fortschritte der Physik 42, 101–141 (1994).
- [8] Matthias Burkardt, Impact parameter space interpretation for generalized parton distributions, International Journal of Modern Physics A 18, 173– 207 (2003).
- [9] H. Mkrtchyan et al., A Prototype of Electromagnetic Calorimeter Constructed of Lead Tungstate, Journal of Contemporary Physics (Armenian Academy of Sciences) 59, 11–16 (2024).
- [10] T. Horn, V.V. Berdnikov, S. Ali, A. Asaturyan, M. Carmignotto, J. Crafts, Alexandre Demarque, R. Ent, G. Hull, H.-S. Ko et al., "Scintillating crystals for the neutral particle spectrometer in Hall C at JLab," Nuclear

345

- Instruments and Methods in Physics Research Section A: Accelerators, Spectrometers, Detectors and Associated Equipment, vol. 956, p. 163375, 2020. Elsevier
- [11] A. Asaturyan, F. Barbosa, V. Berdnikov, E. Chudakov, J. Crafts, H. Egiyan, L. Gan, A. Gasparian, K. Harding, T. Horn et al., "Electromagnetic calorimeters based on scintillating lead tungstate crystals for experiments at Jefferson Lab," Nucl. Instrum. Meth. A, vol. 1013, p. 165683, (2021).
- [12] A. Gasparian, P. Ambrozewicz, R. Pedroni, L. Gan, T. Black, D. Dale, D. Lawrence, E. Smith, A. Somov, M. Khandaker *et al.*, "A precision measurement of the η radiative decay width via the Primakoff effect," *JLAB Experiment E12-10-011, PrimEx note*, No. 57, (2009).
- [13] V. Popov and H. Mkrtchyan, "New photomultiplier active base for Hall C Jefferson Lab lead tungstate calorimeter," in 2012 IEEE Nuclear Science Symposium and Medical Imaging Conference Record (NSS/MIC), IEEE, pp. 1177–1179, (2012).
  - [14] O.K. Baker, J. Beaufait, R. Carlini, J. Cha, S. Danagoulian, A. Johnson, B. Kross, S. Majewski, A. McCauley, W. Naing et al., The high momentum spectrometer drift chambers in Hall C at CEBAF, Nucl. Instrum. Meth. A 367, 92–95 (1995).

375

400

- [15] L. Tang, C. Yan, E.V. Hungerford, Systematic resolution study of the CE-BAF Hall C spectrometersHMS and SOS, Nucl. Instrum. Meth. A 366, 259–262 (1995).
- [16] Carlos Yero, Cross section measurements of deuteron electrodisintegration at very high recoil momenta and large 4-momentum transfers (Q<sup>2</sup>), Ph.D. dissertation, Thomas Jefferson National Accelerator Facility (TJNAF), Newport News, VA, 2020.
  - [17] G.M. Huber *et al.*, "Charged pion form factor between  $Q^2 = 0.60$  and 2.45 GeV<sup>2</sup>. II. Determination of, and results for, the pion form factor", *Phys. Rev. C* **78**, 045203 (2008).
  - [18] T. Horn *et al.*, "Determination of the charged pion form factor at  $Q^2 = 1.60$  and 2.45 GeV<sup>2</sup>", *Phys. Rev. Lett.* **97**, 192001 (2006).
- [19] H. Dong, C. Cuevas, D. Curry, E. Jastrzembski, F. Barbosa, J. Wilson, M. Taylor, and B. Raydo, "Integrated tests of a high speed VXS switch card and 250 MSPS flash ADCs," in *Proceedings of the 2007 IEEE Nuclear Science Symposium Conference Record*, vol. 1, pp. 831–833, IEEE, (2007).
  - [20] M. Wirthlin, "High-reliability FPGA-based systems: Space, high-energy physics, and beyond," *Proc. IEEE*, vol. 103, no. 3, pp. 379–389, (2015).
  - [21] S. Anvar, O. Gachelin, P. Kestener, H. Le Provost, and I. Mandjavidze, "FPGA-based system-on-chip designs for real-time applications in particle physics," *IEEE Trans. Nucl. Sci.*, vol. 53, no. 3, pp. 682–687, (2006).
  - [22] N. Akchurin et al., "Effects of the temperature dependence of the signals from lead tungstate crystals," *Nucl. Instrum. Methods Phys. Res. A*, vol. 593, pp. 530–538, (2008).
  - [23] B. J. Owen and B. S. Sathyaprakash, "Matched filtering of gravitational waves from inspiraling compact binaries: Computational cost and template placement," *Phys. Rev. D*, vol. 60, no. 2, p. 022002, (1999).
- 405 [24] H. Gabbard, M. Williams, F. Hayes, and C. Messenger, "Matching matched filtering with deep networks for gravitational-wave astronomy," *Phys. Rev. Lett.*, vol. 120, no. 14, p. 141103, (2018).
  - [25] S. McKinley and M. Levine, "Cubic spline interpolation," *College of the Redwoods*, vol. 45, no. 1, pp. 1049–1060, (1998).
- 410 [26] T. C. Awes, F. E. Obenshain, F. Plasil, S. Saini, S. P. Sorensen, and G. R. Young, "A simple method of shower localization and identification in laterally segmented calorimeters," *Nucl. Instrum. Meth. Phys. Res.* A, vol. 311, no. 12, pp. 130–138, (1992).
- [27] M. Mazouz, L. Ghedira, and E. Voutier, "Determination of shower central position in laterally segmented lead-fluoride electromagnetic calorimeters," J. Instrum., vol. 11, no. 07, p. P07001, (2016).
  - [28] W. Hamdi, M. Mazouz, and S. Chaibi, "Multilayer perceptron approach for determining the centroid position of the electromagnetic shower in laterally segmented calorimeter," *J. Instrum.*, vol. 20, no. 02, p. T02006, (2025).
  - [29] D. Martinez Santos and F. Dupertuis, "Mass distributions marginalized over per-event errors," *Nucl. Instrum. Methods Phys. Res. A*, vol. 764, pp. 150–155, (2014).
- [30] M. Kubantsev, I. Larin and A. Gasparian, "Performance of the PrimEx Electromagnetic Calorimeter," AIP Conference Proceedings, vol. 867, pp. 51–58, (2006).